

Galaxy Morphologies Revealed with Subaru HSC and Super-Resolution Techniques I: Major Merger Fractions of

$L_{UV} \sim 3 - 15 L_{UV}^*$ Dropout Galaxies at $z \sim 4 - 7^*$

Takatoshi SHIBUYA¹, Noriaki MIURA¹, Kenji IWADATE¹, Seiji FUJIMOTO^{2, 3},
Yuichi HARIKANE^{4, 5}, Yoshiki TOBA^{6, 7, 8}, Takuya UYAHARA¹ and Yohito ITO¹

¹Kitami Institute of Technology, 165, Koen-cho, Kitami, Hokkaido 090-8507, Japan

²Cosmic Dawn Center (DAWN), Jagtvej 128, DK2200 Copenhagen N, Denmark

³Niels Bohr Institute, University of Copenhagen, Lyngbyvej 2, DK2100 Copenhagen Ø, Denmark

⁴Institute for Cosmic Ray Research, The University of Tokyo, 5-1-5 Kashiwanoha, Kashiwa, Chiba 277-8582, Japan

⁵Department of Physics and Astronomy, University College London, Gower Street, London WC1E 6BT, UK

⁶Department of Astronomy, Kyoto University, Kitashirakawa-Oiwake-cho, Sakyo-ku, Kyoto 606-8502, Japan

⁷Academia Sinica Institute of Astronomy and Astrophysics, 11F of Astronomy-Mathematics Building, AS/NTU, No.1, Section 4, Roosevelt Road, Taipei 10617, Taiwan

⁸Research Center for Space and Cosmic Evolution, Ehime University, 2-5 Bunkyo-cho, Matsuyama, Ehime 790-8577, Japan

*E-mail: tshibuya@mail.kitami-it.ac.jp

Received (reception date); Accepted (acceptation date)

Abstract

We perform a super-resolution analysis of the Subaru Hyper Suprime-Cam (HSC) images to estimate the major merger fractions of $z \sim 4 - 7$ dropout galaxies at the bright end of galaxy UV luminosity functions (LFs). Our super-resolution technique improves the spatial resolution of the ground-based HSC images, from $\sim 1''$ to $\lesssim 0''.1$, which is comparable to that of the *Hubble Space Telescope*, allowing us to identify $z \sim 4 - 7$ bright major mergers at a high completeness value of $\gtrsim 90\%$. We apply the super-resolution technique to 6535 very bright dropout galaxies in a UV luminosity range of $L_{UV} \sim 3 - 15 L_{UV}^*$ corresponding to $-24 \lesssim M_{UV} \lesssim -22$. The major merger fractions are estimated to be $f_{\text{merger}} \sim 5 - 20\%$ at $z \sim 4$ and $\sim 50 - 80\%$ at $z \sim 5 - 7$, which shows no f_{merger} difference compared to those of a control faint galaxy sample. Based on the f_{merger} estimates, we verify contributions of source blending effects and major mergers to the bright-end of double power-law (DPL) shape of $z \sim 4 - 7$ galaxy UV LFs. While these two effects partly explain the DPL shape at $L_{UV} \sim 3 - 10 L_{UV}^*$, the DPL shape cannot be explained at the very bright end of $L_{UV} \gtrsim 10 L_{UV}^*$, even after the AGN contribution is subtracted. The results support scenarios in which other additional mechanisms such as insignificant mass quenching effects and the low dust obscuration contribute to the DPL shape of galaxy UV LFs.

Key words: galaxies: structure — galaxies: formation — galaxies: evolution — galaxies: high-redshift

1 Introduction

The shape of the rest-frame ultraviolet (UV) luminosity functions (LFs) provides important clues for understanding physical mechanisms of the galaxy formation and evolution. Extensive searches with the *Hubble Space Telescope* (hereafter, *Hubble*) have identified $> 10,000$ galaxies fainter than an absolute UV magnitude of $M_{\text{UV}} \sim -22$ (e.g., Bradley et al. 2012; Oesch et al. 2010a; Oesch et al. 2013; McLure et al. 2013; Finkelstein et al. 2015; Calvi et al. 2016; McLeod et al. 2016; Parsa et al. 2016; Bouwens et al. 2021 and reference therein), suggesting that galaxy UV LFs at redshifts $z \sim 2-10$ basically follow the Schechter function with the bright-end exponential cut-off in the number density (Schechter 1976). Complementary to these *Hubble* observations, wide-area imaging surveys with ground-based telescopes have uncovered the shape of UV LFs at $z \gtrsim 4$ in a high UV luminosity regime of $-24 \lesssim M_{\text{UV}} \lesssim -23$ where the number density of galaxies and low-luminosity AGNs is comparable (e.g., Ono et al. 2018; Stevans et al. 2018; Akiyama et al. 2018; Matsuoka et al. 2019; Stefanon et al. 2017; Stefanon et al. 2019; Adams et al. 2020; Bowler et al. 2021, Y. Harikane et al. in preparation). The most intriguing feature in the bright-end shape of galaxy UV LFs is that the number density at $-24 \lesssim M_{\text{UV}} \lesssim -23$ could deviate from the Schechter functions even if the AGN contribution is subtracted based on spectroscopic data and/or the source extendedness. The bright-end number density excess of galaxy UV LFs has been often characterized by the double power-law (DPL) function with $M_{\text{UV}} \lesssim -22$ bright and $M_{\text{UV}} \gtrsim -21$ faint power-law slopes (e.g., Bowler et al. 2012; Bowler et al. 2014). Several scenarios have been proposed to explain the bright-end DPL shape of galaxy UV LFs at high redshifts: 1) insignificant mass quenching (e.g., Binney 1977; Croton et al. 2006; Peng et al. 2010; Ren et al. 2019), 2) low dust obscuration (Bowler et al. 2015; Bowler et al. 2020), 3) gravitational lensing magnification (e.g., Wyithe et al. 2011; Takahashi et al. 2011; Mason et al. 2015; Barone-Nugent et al. 2015), and 4) galaxy selection and analysis biases related to measurements of redshifts and source extendedness (e.g., Adams et al. 2020).

In addition to these scenarios, galaxy mergers could play significant roles in shaping the bright end of galaxy

UV LFs by two effects: 1) the source blending effect and 2) the star-formation rate (SFR) enhancement. Individual galaxy components of a merger system tend to be blended at the low spatial resolution, in which case the blended sources are considered as bright single galaxies (e.g., Bowler et al. 2017). On the other hand, the UV luminosity could be brighten as a consequence of the SFR enhancement caused by galaxy mergers and interactions (e.g., Ellison et al. 2008; Wong et al. 2011; Ellison et al. 2013; Behroozi et al. 2015; Cibinel et al. 2019). The predominance of major mergers at high- z might influence the fraction of bright galaxies (e.g., Ostriker & Tremaine 1975; Sawicki et al. 2020). These effects might reproduce the DPL functional form by flattening the bright-end exponential decline of the Schechter function. However, it is difficult to investigate the morphology of $z \gtrsim 4$ bright galaxies at the sub-structure level of merging systems with low spatial resolution images of ground-based telescopes. Follow-up observations with *Hubble* are a promising approach (e.g., Jiang et al. 2013; Willott et al. 2013; Bowler et al. 2017), but unable to be efficiently performed for bright galaxies that are patchy distributed over $\gtrsim 100$ -deg²-scale wide-area survey fields. For the reason, image processing techniques (e.g., super-resolution and machine learning) are critical to address such questions about morphological properties with a statistical sample of high- z bright galaxies.

In this paper, we study the relation between the bright-end shape of UV LFs and galaxy mergers with a super-resolution technique and the Subaru/Hyper Suprime-Cam (HSC)-Strategic Survey Program (SSP) data (Aihara et al. 2018a; Aihara et al. 2018b; Miyazaki et al. 2012; Miyazaki et al. 2018; Komiyama et al. 2018; Kawanomoto et al. 2018; Furusawa et al. 2018). This is the first paper in a series investigating the galaxy morphology with techniques of the super-resolution. The structure of this paper is as follows. We describe details of the HSC-SSP data and dropout galaxy samples in Section 2. Section 3 explains the super-resolution technique, a method to identify galaxy mergers, the completeness and the contamination rate for the galaxy merger identification, and how to estimate galaxy merger fractions. In Section 4, we present the galaxy merger fractions for bright dropout galaxies. In Section 5, we discuss the possibility that the number density excess is reproduced by galaxy mergers. Section 6 summarizes our findings.

* Based on data collected at the Subaru Telescope and retrieved from the HSC data archive system, which is operated by Subaru Telescope and Astronomy Data Center at National Astronomical Observatory of Japan.

Table 1. Sample of Bright Dropout Galaxies for Our Super-Resolution Study*

Redshift	Field	m_{UV} (mag)	M_{UV} (mag)	L_{UV}/L_{UV}^*	N_{gal}
(1)	(2)	(3)	(4)	(5)	(6)
4	UltraDeep	22.00 – 23.69	–23.94 – (–22.25)	15.00 – 3.16	60
	Deep	21.94 – 23.69	–24.00 – (–22.25)	15.85 – 3.16	1038
	Wide	22.90 – 23.69	–23.04 – (–22.25)	6.55 – 3.16	5314
5	UltraDeep	21.87 – 23.59	–24.50 – (–22.77)	25.12 – 5.11	3
	Deep	23.37 – 23.59	–22.99 – (–22.77)	6.25 – 5.11	13
	Wide [†]	—	—	—	—
6	UltraDeep	22.67 – 23.94	–24.00 – (–22.73)	15.85 – 4.92	0
	Deep	22.67 – 23.94	–24.00 – (–22.73)	15.85 – 4.92	14
	Wide	22.67 – 23.94	–24.00 – (–22.73)	15.85 – 4.92	80
7 [#]	UltraDeep ^{††}	—	—	—	—
	Deep	< 24.50	< –22.41	> 3.66	1
	Wide	< 24.50	< –22.41	> 3.66	12
Total	—	—	—	—	6535

* (1) Redshift of dropout galaxies. (2) Layers of the HSC-SSP fields.

(3) Range of apparent UV magnitude. (4) Range of absolute UV magnitude.

(5) Range of UV luminosity in units of L_{UV}^* . (6) Number of dropout galaxies.

[#] The bright magnitude limit is not placed due to no estimate of galaxy fraction. See Ono et al. (2018).

[†] The m_{UV} range cannot be defined due to a relatively-high contamination fraction of low- z interlopers (i.e., > 50%) at $M_{UV} < M_{UV,th}$. See Section 2 in this paper and Figure 5 in Ono et al. (2018).

^{††} No dropout galaxies are identified in Ono et al. (2018).

Throughout this paper, we assume a flat universe with the cosmological parameters of $(\Omega_m, \Omega_\lambda, h) = (0.3, 0.7, 0.7)$. All magnitudes are given in the AB system (Oke 1974; Oke & Gunn 1983).

2 Data

We use a sample of dropout galaxies at $z \sim 4 - 7$ (Ono et al. 2018; Harikane et al. 2018; Toshikawa et al. 2018). The dropout galaxies are selected with the ~ 100 deg²-area S16A data of the HSC-SSP survey (Aihara et al. 2018a; Aihara et al. 2018b). The sample contains a large number of bright dropout galaxies with $M_{UV} \lesssim -23$, which enables us to study morphological properties of sources at the bright end of galaxy UV LFs. From the sample, we select bright dropout galaxies with the number-density excess. Ono et al. (2018) have obtained two functional forms of galaxy UV LFs by fitting Schechter and DPL functions to the number density of dropout galaxies. Based on the best-fit Schechter and DPL functions, we determine a threshold of UV magnitude $M_{UV,th}$ where the number density of the DPL functions is 0.1 dex larger than that of the Schechter functions. The $M_{UV,th}$ values range from $M_{UV,th} \sim -23$ to $M_{UV,th} \sim -22$ (corresponding to $L_{UV,th} \sim 3 - 5 L_{UV}^*$) which depend on the redshift of

dropout galaxies. In this study, we define sources whose UV magnitude is brighter than $M_{UV,th}$ as “*bright dropout galaxies*”. To reduce contaminations in the sample, we exclude 1) $z \sim 4$ bright dropout galaxies with $m_{UV} < 22.0$ in the HSC-SSP UltraDeep fields because these bright sources are likely to be low- z interlopers (see Section 4.1 of Ono et al. 2018), 2) $z \sim 4 - 5$ bright dropout galaxies with m_{UV} where the contamination fractions of low- z interlopers exceed $\sim 50\%$ (see Section 3.2 of Ono et al. 2018), 3) bright objects in an M_{UV} range where the galaxy fraction is 0% estimated with a spectroscopic sample of Ono et al. (2018), and 4) AGN-like compact sources with the magnitude difference $m_{PSF} - m_{CModel} < 0.15$ (Matsuoka et al. 2019), where m_{PSF} and m_{CModel} are the magnitudes measured with the point spread function (PSF) and the CModel profiles, respectively (see Aihara et al. 2018a for details). Using these selection criteria, we select 6412 at $z \sim 4$, 16 at $z \sim 5$, 94 at $z \sim 6$, and 13 at $z \sim 7$. The total number of the bright dropout galaxies is 6535. For the photometric sample of dropout galaxies, we regard $z = 3.8$, $z = 4.9$, $z = 5.9$, and $z = 6.9$ as each representative redshift which is identical to the assumption in Ono et al. (2018).

As a control sample, we randomly select “*faint dropout galaxies*” in a UV luminosity of $L_{UV} \sim 2.5 L_{UV}^*$ where L_{UV}^* is the characteristic UV luminosity at $z \sim 3$ corresponding

to $M_{UV} = -21$ (Steidel et al. 1999). The number of the faint dropout galaxies is 880 at $z \sim 4$, 748 at $z \sim 5$, and 10 at $z \sim 6$. Note that faint dropout galaxies with $L_{UV} \sim 2.5 L_{UV}^*$ have not been identified at $z \sim 7$ in Ono et al. (2018).

The magnitude, luminosity, and numbers of the sample dropout galaxies are summarized in Table 1.

3 Analysis

3.1 Super-resolution

For our super-resolution analysis, we employ the Richardson-Lucy (RL) deconvolution (Richardson 1972; Lucy 1974). The RL deconvolution is a classical maximum-likelihood algorithm simply assuming that the noise of an observed image \mathbf{y} ,

$$\mathbf{y} = p(\mathbf{P}\mathbf{x}), \quad (1)$$

follows Poisson statistics p at a specific image pixel i ,

$$p(\mathbf{y}_i|\mathbf{x}) = \frac{(\mathbf{P}\mathbf{x})_i^{y_i} e^{-(\mathbf{P}\mathbf{x})_i}}{y_i!}, \quad (2)$$

where \mathbf{P} is a PSF matrix, and \mathbf{x} is a vector of a restored image. It is well known that the RL deconvolution yields a super-resolution effect because the cutoff spatial frequency of the image \mathbf{x} gradually increases during the maximum likelihood estimation. While the RL deconvolution algorithm has been widely used in many applications, especially for the image de-noising, this technique has been scarcely applied to studies of high- z galaxies. One advantage to use this algorithm is no requirement of large training samples that are commonly prepared for recent machine learning-based studies. Only observed object and PSF images are needed for the RL deconvolution

To make the optimization of the RL deconvolution stable and efficient, we exploit the Alternating Direction Method of Multipliers (ADMM) algorithm (Boyd et al. 2011). We minimize the following two penalty functions,

$$\underset{\{\mathbf{x}\}}{\text{minimize}} \quad -\log\{p(\mathbf{y}|\mathbf{w}_1)\} + I_{R_+}(\mathbf{w}_2) \quad (3)$$

$$\text{subject to } \mathbf{A}\mathbf{x} - \mathbf{w} = 0, \quad \mathbf{A} = \begin{bmatrix} \mathbf{P} \\ \mathbf{I} \end{bmatrix}, \quad \mathbf{w} = \begin{bmatrix} \mathbf{w}_1 \\ \mathbf{w}_2 \end{bmatrix}$$

where the first term $-\log\{p(\mathbf{y}|\mathbf{w}_1)\}$ is the maximum likelihood estimator for the Poisson noise, the second term $I_{R_+}(\mathbf{w}_2)$ is the indicator function defined as the following Equation (4), and \mathbf{I} is the identity matrix. The \mathbf{w}_1 and \mathbf{w}_2 vectors are new auxiliary variables for the terms of the Poisson noise and the flux non-negativity, respectively.

$$I_{R_+}(w) = \begin{cases} 0 & w \in R_+ \\ +\infty & w \notin R_+ \end{cases} \quad (4)$$

where R_+ is the closed nonempty convex set of the flux non-negativity constraints.

We formulate the Augmented Lagrangian as

$$L_\rho(\mathbf{x}, \mathbf{w}, \mathbf{h}) = -\log\{p(\mathbf{y}|\mathbf{w}_1)\} + I_{R_+}(\mathbf{w}_2) + \mathbf{h}^T(\mathbf{A}\mathbf{x} - \mathbf{w}) + \frac{\rho}{2}\|\mathbf{A}\mathbf{x} - \mathbf{w}\|_2^2 \quad (5)$$

where \mathbf{h} is the Lagrange multiplier, and ρ is a parameter for the rate of the ADMM updates. Based on a parameter search for ρ , we choose $\rho = 1 \times 10^{-3}$ for the stable and fast convergence, although the ρ value does not significantly affect results of the super-resolution. Using the ADMM algorithm, we divide the problem of the RL deconvolution into subproblems, update iteratively the $(\mathbf{x}, \mathbf{w}_1, \mathbf{w}_2, \mathbf{h})$ vectors, and obtain a super-resolution image \mathbf{x} in a method similar to those of, e.g., Figueiredo & Bioucas-Dias (2010) and Wen et al. (2016). Section 7 presents details of how to solve each subproblem.

For the convergence check during the iteration, we monitor the total absolute percentage error,

$$E(n_{\text{iter}}) = \sum_{i=1}^{N_{\text{im}}} \frac{|P_i * x_i - y_i|}{|y_i|} \quad (6)$$

where $*$ denotes the convolution operator, i is a specific pixel, n_{iter} is the current iteration number, and N_{im} is the total number of image pixels. We force the iteration to stop when the super-resolution image \mathbf{x} meets a convergence criterion of $|dE(n_{\text{iter}})/dn_{\text{iter}}| < 1 \times 10^{-3}$ at least 10 times consecutively, or n_{iter} exceeds $N_{\text{iter}} = 250$.

A number of recent studies have introduced other regularization terms of, e.g., the total variation (Rudin et al. 1992) and the L1 norm (Tibshirani 1996). To avoid tuning parameters for such regularization terms, we use only the two penalty functions related to the Poisson noise and the flux non-negativity (Equation 3). These two penalty functions are sufficient to resolve compact and faint components of high- z galaxy mergers (Section 3.2).

3.2 Identification of galaxy mergers

Using the super-resolution technique, we analyze the HSC-SSP images to identify galaxy mergers. The super-resolved images are obtained in the following steps. First, we retrieve $96 \text{ pixels} \times 96 \text{ pixels}$ ($16'' \times 16''$) cutout HSC S20A coadd images at the position of each dropout galaxy (Aihara et al. 2019). These HSC-SSP S20A data have been obtained in observations during March 2014 through January 2020, and have been reduced with the `hscPipe` 8.0-8.4 software (Bosch et al. 2018; see also Axelrod et al. 2010; Jurić et al. 2017; Ivezić et al. 2019). We also extract PSF images for each galaxy with the `HSC PSF picker`

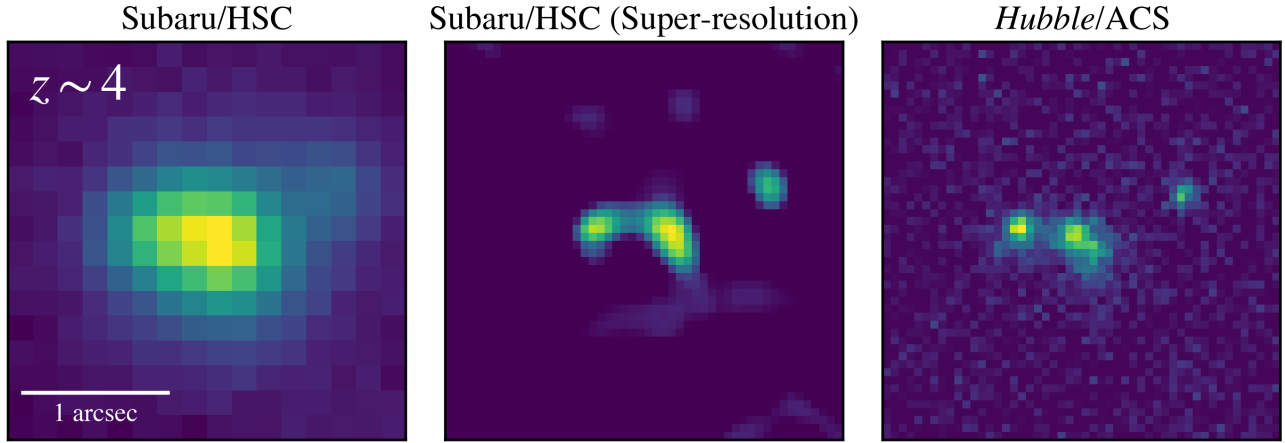


Fig. 1. Images of an example galaxy at $z \sim 4$ analyzed in our super-resolution technique. (Left) Original HSC i -band image. (Middle) Super-resolved HSC i -band image. (Right) *Hubble* I_{814} -band image. The white horizontal bar indicates $1''$.

tool¹. We use images of i -band for $z \sim 4$ g -dropout, z -band for $z \sim 5$ r -dropout, and y -band for $z \sim 6 - 7$ i -dropout galaxies to trace the rest-frame UV continuum emission. The choice of these wavebands is the same as the ones used for galaxy UV LFs of Ono et al. (2018). Second, we magnify the pixels of HSC coadd and PSF images by a factor of 2.8 to match the pixel scale to that of *Hubble* (i.e., $0''.06$ per pixel). Finally, we super-resolve the HSC coadd images in the technique described in Section 3.1. Figures 1 and 2 show examples of super-resolved and de-noised HSC images together with corresponding *Hubble* images, which demonstrates the performance of our super-resolution technique. Our super-resolution technique clearly reveals galaxy sub-structures, e.g., candidates of galaxy merger components, in a scale smaller than the PSF FWHM of HSC (i.e., $\sim 0''.6 - 1''.0$).

From the super-resolved cutout HSC images, we detect sources with the **SExtractor** software (Bertin & Arnouts 1996). The detection parameters of **SExtractor** are set to `DETECT_MINAREA= 5`, `DETECT_THRESH= 2.5`, `ANALYSIS_THRESH= 5.0`, `DEBLEND_NTHRESH= 16`, `DEBLEND_MINCONT= 0.0001`, `PHOT_AUTOPARAMS= 2.5, 3.5`, `SATUR_LEVEL= 120.0`, `MAG_GAMMA= 4.0`, `GAIN= 2.0` which are similar to those of Guo et al. (2013) for the *Hubble* CANDELS GOODS-S data.

In the source catalogs constructed with **SExtractor**, we select galaxy mergers. In this study, we focus only on major mergers with similar-mass components, because it is relatively difficult to differentiate galaxy minor mergers from clumpy galaxies (e.g., Shibuya et al. 2016). Hereafter, the major merger is referred to as simply the “galaxy merger”, otherwise specified. We define galaxy close-pairs with a flux ratio of $\mu = f_2/f_1 \geq 1/4$ and a source separation

within $d = r_{\min} - r_{\max} = 3 - 6.5$ kpc as galaxy mergers, where f_1 and f_2 are the flux for the bright primary and the faint secondary galaxy components, respectively. The criterion of μ is the same as that of most previous studies on major mergers (see, e.g., Table 5 of Mantha et al. 2018, a summary table of previous studies). The criterion of source separation is different from that of previous studies for $z \sim 0 - 3$ (typically $d = 5 - 30$ kpc or $d = 14 - 43$ kpc). The small value of $d = 3 - 6.5$ kpc is adopted for two reasons: i) our criterion of source separation is roughly comparable to that of studies on high- z dropout galaxies (e.g., Jiang et al. 2013; Willott et al. 2013; Bowler et al. 2017), ii) one of our main objectives is to examine the source blending effect on the DPL shape of galaxy UV LFs (see Section 1). We aim to resolve high- z galaxy mergers with such a small source separation which are blended at the ground-based resolution.

3.3 Completeness and Contamination Rate

We estimate the completeness F_{comp} and contamination rate F_{cont} in identifying galaxy mergers. The completeness F_{comp} is a true positive rate or sensitivity which is defined as

$$F_{\text{comp}} = \frac{N_{\text{true}}}{N_{\text{real-merger}}} \quad (7)$$

where N_{true} is the number of objects that are correctly selected as galaxy mergers in our analysis, and $N_{\text{real-merger}}$ is the total number of real mergers. The contamination rate F_{cont} is a false positive rate or fall-out which is defined as

$$F_{\text{cont}} = \frac{N_{\text{false}}}{N_{\text{isolated}}} \quad (8)$$

where N_{false} is the number of isolated galaxies that are

¹ <https://hsc-release.mtk.nao.ac.jp/doc/index.php/tools-2/>

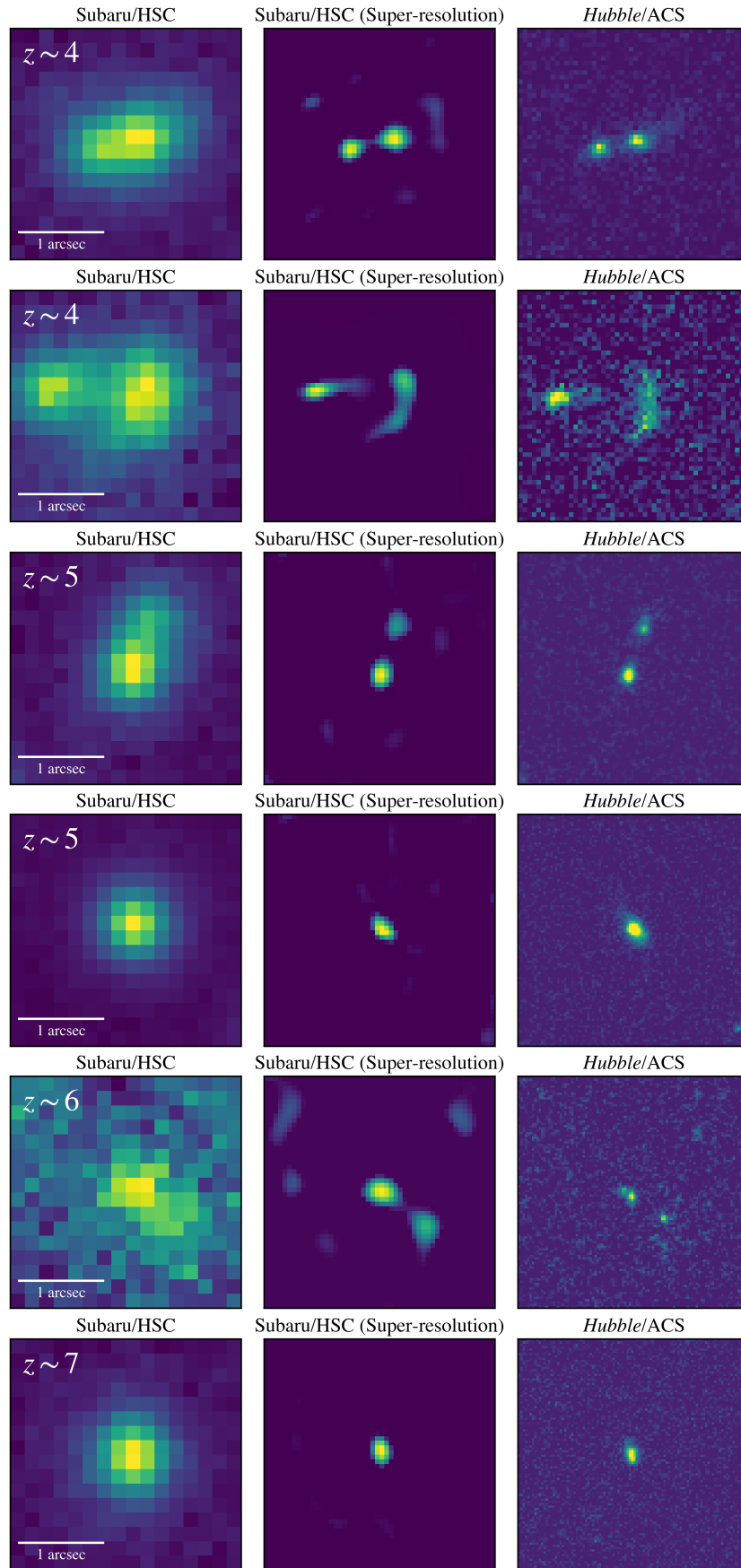


Fig. 2. Same as Figure 1, but for other example galaxies at $z \sim 4 - 7$. Note that the pixel scales of the *Hubble* images for $z \sim 5 - 7$ are different from the original. See Section 3.3 for details.

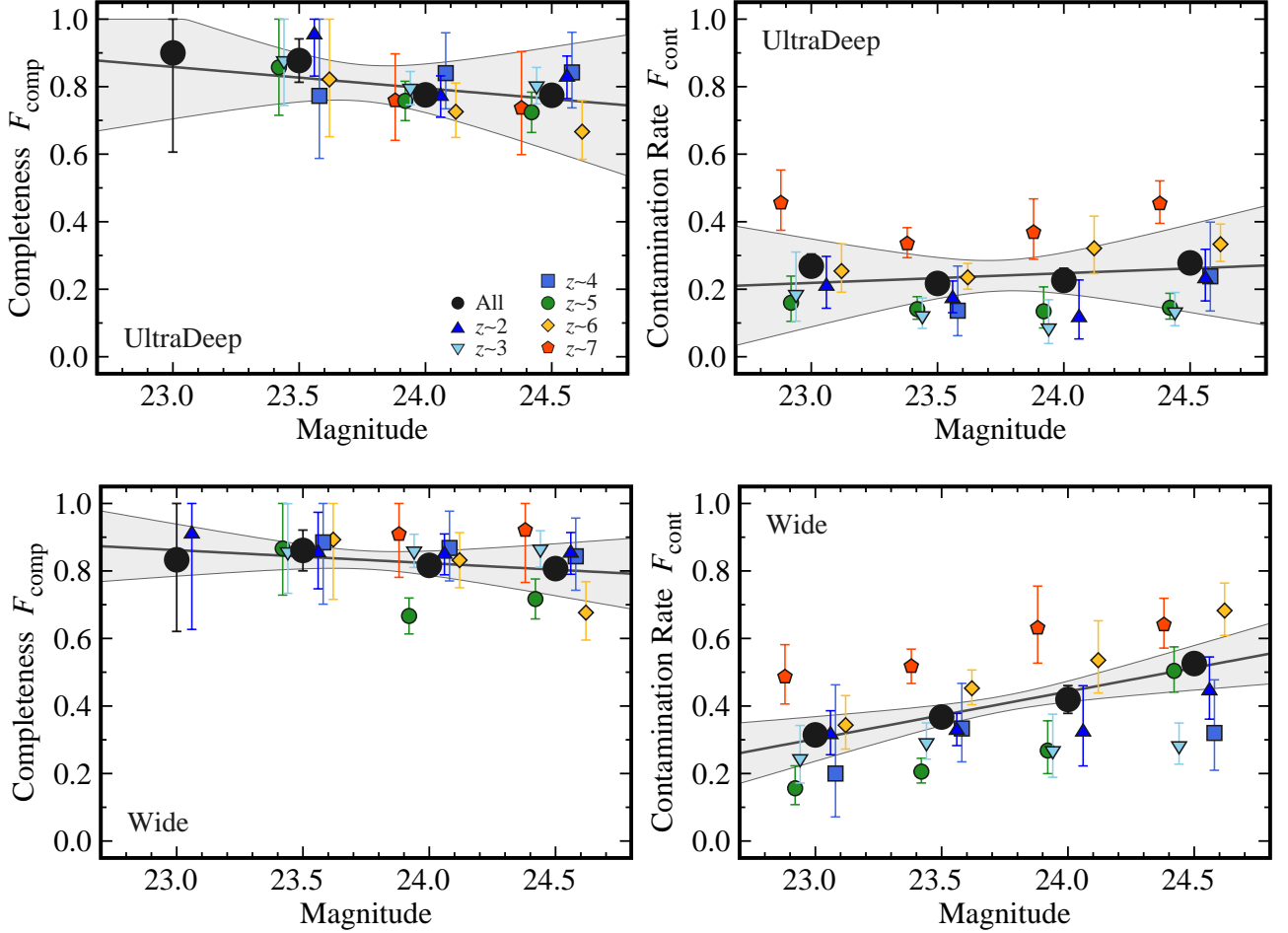


Fig. 3. Completeness (left) and contamination rate (right) as a function of magnitude. The top and bottom panels denote the UltraDeep and Wide fields, respectively. The symbols indicate the completeness and contamination rate estimated for sources at all redshifts (black circles), $z \sim 2$ (blue triangles), $z \sim 3$ (cyan inverse triangles), $z \sim 4$ (blue squares), $z \sim 5$ (green circles), $z \sim 6$ (yellow diamonds), and $z \sim 7$ (red pentagons). The panels show the completeness and contamination rate estimated with at least 10 galaxies in each magnitude bin. The error bars of each symbol are calculated based on Poisson statistics from the galaxy number counts. The black solid lines and shaded gray regions depict the best-fit linear functions with 1σ significance errors to the measurements for all redshifts (i.e., black circles).

incorrectly selected as galaxy mergers in our analysis, and N_{isolated} is the total number of isolated galaxies.² As shown in Figures 1 and 2, some galaxy sub-structures are not clearly reproduced, and faint fake components are emerged in the super-resolved HSC images. The F_{comp} and F_{cont} values are essential to estimate the major merger fractions with our super-resolution technique.

To estimate F_{comp} and F_{cont} , we prepare ground-truth images of galaxy mergers and isolated galaxies. The part of the HSC-SSP UltraDeep COSMOS field has been observed with the *Hubble*/Advanced Camera for Survey (ACS) I_{814} filter, which enables us to compare the super-resolved HSC images with the *Hubble* ones. By using a detection source

catalog of Leauthaud et al. (2007) constructed for the *Hubble* COSMOS-Wide data and the HSC-SSP MIZUKI photometric redshifts (Tanaka et al. 2018), we select galaxy mergers and isolated galaxies at $z > 2$. Here, we apply the same selection criteria of the flux ratio and source separation as those for the dropout galaxies (Section 3.2). The numbers of selected galaxy mergers and isolated galaxies are $\sim 1,500$ and $\sim 1,100$, respectively. In the same manner as that for the dropout galaxies, we analyze the HSC i -band images for galaxies at $z \sim 2, 3$, and 4.

Because of no wide-area *Hubble* data covered by wavelength ranges of HSC z and y bands, we artificially create HSC z - and y -band images for galaxies at $z \sim 5, 6$, and 7. First, we shrink the super-resolved HSC i -band images of galaxies at $z \sim 2, 3$, and 4. The shrinkage factor is determined from the galaxy size evolution of $r_e \sim (1+z)^{-1.2}$ (Shibuya et al. 2015). Second, we convolve these shrunk

² In object classification studies with machine learning techniques, the contamination rate is often defined as $F_{\text{cont}} = N_{\text{false}} / (N_{\text{true}} + N_{\text{false}})$. In this study, we use the definition of F_{cont} which is the same as that of previous studies on galaxy mergers (e.g., Lackner et al. 2014).

images with the randomly-selected z - and y -band PSF images. Finally, these PSF-convolved images are embedded into z - and y -band sky regions in the HSC-SSP UltraDeep and Wide fields to add the real sky background noise. As in the HSC i -band images, we estimate F_{comp} and F_{cont} for galaxies at $z \sim 5, 6$, and 7 .

Figure 3 shows F_{comp} and F_{cont} as a function of magnitude. Even with the relatively low spatial resolution images of the ground-based Subaru telescope, our super-resolution technique successfully identifies galaxy mergers at a high completeness of $F_{\text{comp}} \gtrsim 90\%$ and a low contamination rate of $F_{\text{cont}} \lesssim 20\%$ at bright magnitude $m \lesssim 23$. Given that the dropout galaxies are bright (i.e., $m \sim 22 - 24$, see Table 1), the major merger fraction can be estimated at high F_{comp} and relatively low F_{cont} values. Although F_{comp} and F_{cont} do not largely change with magnitude, F_{comp} (F_{cont}) slowly decreases (increases) toward faint magnitudes. There is no strong dependence of F_{comp} and F_{cont} on image depths (i.e., UltraDeep or Wide).

To obtain functional forms of F_{comp} and F_{cont} , we fit a linear function to the data points of all-redshift galaxies (i.e., black circles). As shown in Figure 3, most data points are distributed within the 1σ error regions of the best-fit F_{comp} and F_{cont} linear functions. Because of this consistency, we assume that F_{comp} and F_{cont} at any redshifts follow the best-fit linear functions. The linear functions for the Deep fields are calculated from the depth-weighted average of the results for the UltraDeep and Wide fields.

3.4 Estimate of Major Merger Fraction

In this section, we describe how to estimate the major merger fraction. The major merger fraction is calculated as

$$f_{\text{merger}} = \frac{N_{\text{merger}}}{N} \quad (9)$$

where N_{merger} and N are the numbers of major merger systems and dropout galaxies, respectively.³ The N_{merger} value is obtained from N_{selected} which is the number of major merger systems selected in the selection criteria of $\mu \geq 1/4$ and $d = r_{\text{min}} - r_{\text{max}} = 3 - 6.5$ kpc (see Section 3.2). In the same manners as that of Cotini et al. (2013), we correct N_{selected} for the incompleteness and contamination in identifying galaxy mergers. Using F_{comp} and F_{cont} estimated in Section 3.3, N_{merger} is derived as

$$N_{\text{merger}} = \frac{N_{\text{selected}} - F_{\text{cont}}N}{F_{\text{comp}} - F_{\text{cont}}}. \quad (10)$$

The major merger fractions derived in Equations (9) and (10) are presented in Column (2) of Table 2.

³ The definition corresponds to the pair fraction f_{pair} (e.g., Bundy et al. 2009).

In addition to the incompleteness and contamination, we take into account the chance projection of foreground/background sources. Our method of identifying galaxy mergers relies on the projected separation with no redshift information of each galaxy component. Thus, foreground/background sources can be observed, by chance, near isolated galaxies. Following methods of e.g., Le Fèvre et al. (2000), Patton et al. (2000), Bundy et al. (2009), Bluck et al. (2009), and Bluck et al. (2012), we correct for the chance projection effect by calculating

$$f_{\text{merger}} = \frac{N_{\text{merger}} - N_{\text{proj}}}{N} \quad (11)$$

where N_{proj} is the expected number of chance projection sources in a galaxy sample. The expected number of chance projection sources per galaxy is obtained by multiplying the area of the major merger search annulus $\pi(r_{\text{max}}^2 - r_{\text{min}}^2)$ by the average surface number density of galaxies S in the flux interval $0.25f_1 \leq f < f_1$. To estimate S , we extract extended sources (i.e., galaxies) in the HSC-SSP UltraDeep COSMOS field by setting the (i, z, y)_extendedness_value flag to 1 (Aihara et al. 2018b).

Column (3) of Table 2 summarizes the major merger fractions corrected for all of the incompleteness, the contamination, and the chance projection effect. Note that we have included their uncertainties related to F_{comp} , F_{cont} , and/or the Poisson error of N_{proj} to f_{merger} in Table 2. Even if we take into account the chance projection effect, the correction changes f_{merger} by only $\sim 5 - 20\%$. This is because the small area of search annulus reduces the probability of the chance projection.

In the next sections, we basically use f_{merger} corrected for all of the incompleteness, the contamination, and the chance projection effect (i.e., Column 3 of Table 2), otherwise specified. For the discussion about the source blending effect on galaxy UV LFs (Section 5.1), we adopt f_{merger} in Column (2) of Table 2.

4 Results

4.1 Major Merger Fraction as a Function of M_{UV}

Figure 4 presents the major merger fractions as a function of M_{UV} for dropout galaxies at $z \sim 4 - 7$. The combination of the wide-area HSC-SSP data with our super-resolution technique reveals f_{merger} in the number density excess regime of $M_{\text{UV}} \lesssim -22.2$ ($L_{\text{UV}} \gtrsim 3L_{\text{UV}}^*$) of galaxy UV LFs. Among the redshifts of $z \sim 4 - 7$, the $z \sim 4$ galaxy sample covers the widest absolute UV magnitude range of $-24 \lesssim M_{\text{UV}} \lesssim -22.2$ corresponding to $L_{\text{UV}} \sim 3 - 15 L_{\text{UV}}^*$. We find that f_{merger} at $z \sim 4$ is almost constant at $\sim 5 - 20\%$ in the M_{UV} range, but shows a mild decreasing trend toward bright M_{UV} . Albeit with relatively large error bars

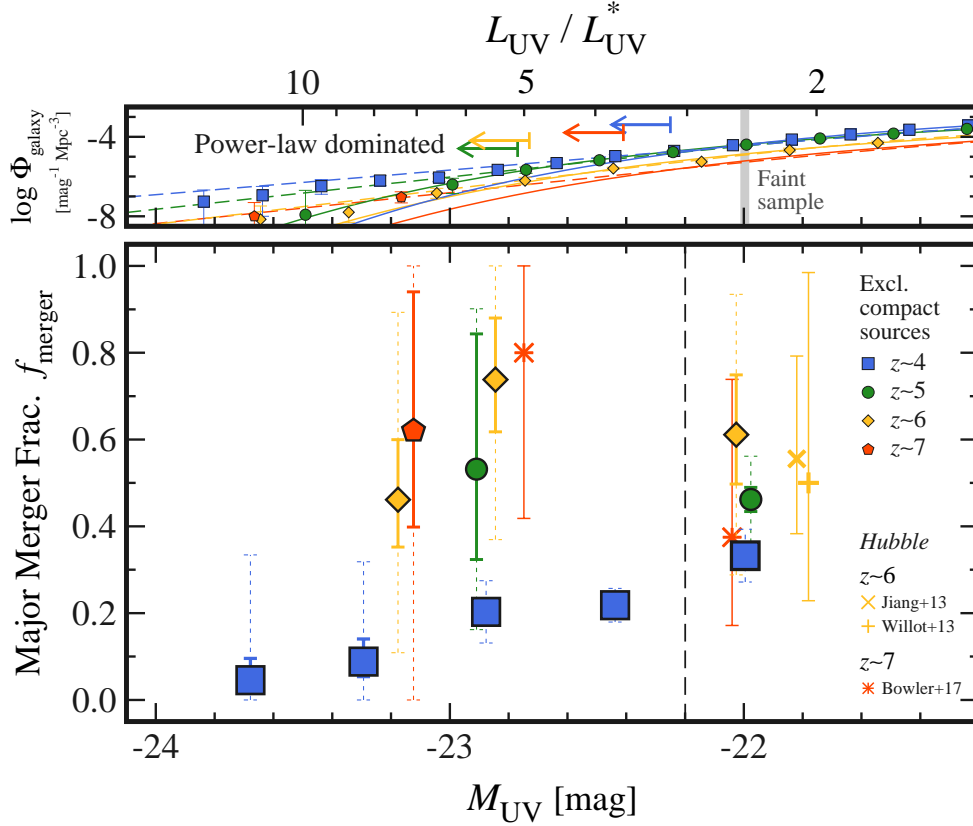


Fig. 4. Major merger fraction as a function of absolute UV magnitude. The filled symbols present dropout galaxies at $z \sim 4$ (blue squares), $z \sim 5$ (green circles), $z \sim 6$ (yellow diamonds), and $z \sim 7$ (red pentagons). In the f_{merger} estimates for these filled symbols, compact sources are excluded with a selection criterion of magnitude difference $m_{\text{PSF}} - m_{\text{CModel}} < 0.15$ (Matsuoka et al. 2019). Dropout galaxies in previous *Hubble* studies are plotted (yellow cross: $z \sim 6$ in Jiang et al. 2013; yellow plus mark: $z \sim 6$ in Willott et al. 2013; red asterisks: $z \sim 7$ in Bowler et al. 2017). The f_{merger} values of Bowler et al. (2017) are calculated for dropout galaxies in ranges of $M_{\text{UV,th}} \lesssim -22.41$ and $M_{\text{UV}} = -22.0 \pm 0.4$ by assuming that sources with multiple distinct components are major mergers. The absolute UV magnitude of the dropout galaxies in Jiang et al. (2013) and Willott et al. (2013) are assumed to be $M_{\text{UV}} \sim -21.8$. The thick solid error bars of ours and the previous *Hubble* studies are calculated based on Poisson statistics from the galaxy number counts. In addition to the Poisson error, the thin dashed error bars include the uncertainties related to the incompleteness and contamination in the galaxy merger identification and the galaxy chance projection effect. The vertical dashed line is depicted for the division between the bright and faint galaxy samples. The data points are slightly offset along the x axis for clarity. The top panel indicates the galaxy UV luminosity functions at $z \sim 4 - 7$ from Ono et al. (2018). The solid and dashed curves correspond to the best-fit Schechter and DPL functions, respectively, with the color coding the same as for the symbols. The AGN contribution has been subtracted from these galaxy UV luminosity functions. The arrows indicate the UV luminosity regime where the number density of the DPL functions is 0.1 dex higher than that of the Schechter functions. The vertical gray line denotes the luminosity of the faint galaxy sample, $L_{\text{UV}} \sim 2.5 L_{\text{UV}}^*$. The top x axis represents the corresponding UV luminosity in units of L_{UV}^* .

at higher redshifts due to the small sample size, f_{merger} seem to increase from $z \sim 4$ to $z \sim 5 - 7$. The redshift evolution of f_{merger} is examined in details in Section 4.2. At each redshift, there is no enhancement in f_{merger} for the bright dropout galaxy sample compared to those for the corresponding control faint dropout galaxy sample, by considering the uncertainties. The no enhancement in f_{merger} would imply the major merger is not a dominant source for the bright-end DPL shape of galaxy UV LFs (Section 5). A similar result on f_{merger} is obtained in our machine learning-based study, which will be presented in a companion paper.

We compare f_{merger} estimated for our 6535 bright dropout galaxies with those of previous *Hubble* studies. As

described below, our f_{merger} estimates are consistent with those of the previous *Hubble* studies within the 1σ uncertainty. Due to the small field of view (FoV) of *Hubble*, there have been few statistical studies on the morphology of high- z galaxies with $M_{\text{UV}} \lesssim -22$ at the sub-structure level of merging systems (see, e.g., Ravindranath et al. 2006; Lotz et al. 2006; Conselice & Arnold 2009; Oesch et al. 2010b; Kawamata et al. 2015; Curtis-Lake et al. 2016 for faint galaxies at $z \gtrsim 4$; see also ALMA studies on f_{merger} with [C II]158 μm line maps, e.g., Le Fèvre et al. 2020). Despite of the small FoV, some studies have examined the morphology of bright dropout galaxies by using the existing *Hubble* data of, e.g., CANDELS (Grogin et al. 2011; Koekemoer et al. 2011) or by conducting multiple

Table 2. Major merger fractions as a function of M_{UV}^*

M_{UV} (mag)	f_{merger} ($F_{\text{comp}}, F_{\text{cont}}$) -corrected	f_{merger} ($F_{\text{comp}}, F_{\text{cont}}, N_{\text{proj}}$) -corrected
(1)	(2)	(3)
$z \sim 4$		
-23.68	$0.06^{+0.05}_{-0.03}$ (+0.29, -0.06)	$0.05^{+0.05}_{-0.03}$ (+0.29, -0.05)
-23.29	$0.10^{+0.05}_{-0.04}$ (+0.23, -0.10)	$0.09^{+0.05}_{-0.03}$ (+0.23, -0.09)
-22.88	$0.22^{+0.02}_{-0.02}$ (+0.07, -0.07)	$0.20^{+0.02}_{-0.02}$ (+0.07, -0.07)
-22.44	$0.25^{+0.01}_{-0.01}$ (+0.04, -0.04)	$0.22^{+0.01}_{-0.01}$ (+0.04, -0.04)
$z \sim 5$		
-22.87	$0.56^{+0.32}_{-0.21}$ (+0.35, -0.35)	$0.53^{+0.31}_{-0.21}$ (+0.37, -0.37)
$z \sim 6$		
-23.18	$0.51^{+0.14}_{-0.11}$ (+0.43, -0.35)	$0.46^{+0.14}_{-0.11}$ (+0.43, -0.35)
-22.84	$0.79^{+0.15}_{-0.13}$ (+0.36, -0.36)	$0.74^{+0.14}_{-0.12}$ (+0.26, -0.37)
$z \sim 7$		
-23.12	$0.70^{+0.30}_{-0.24}$ (+0.30, -0.70)	$0.62^{+0.32}_{-0.22}$ (+0.38, -0.62)

* (1) Absolute UV magnitude. (2) Major merger fraction corrected for the incompleteness and contamination in the major merger identification. (3) Major merger fraction corrected for the incompleteness and contamination in the major merger identification and the chance projection effect. In the columns (2) and (3), the errors are based on Poisson statistics. In addition to the Poisson error, the values in parenthesis include the uncertainties related to F_{comp} , F_{cont} , and N_{proj} .

Table 3. Major merger fractions as a function of redshift*

Redshift (1)	f_{merger} (2)
4	$0.21^{+0.02}_{-0.02}$ (+0.08, -0.08)
5	$0.54^{+0.35}_{-0.23}$ (+0.41, -0.41)
6	$0.63^{+0.13}_{-0.11}$ (+0.32, -0.32)
7	$0.81^{+0.19}_{-0.28}$ (+0.19, -0.81)

* (1) Redshift. (2) Major merger fraction in a narrow UV magnitude range $-23.4 < M_{UV} < -22.8$. The f_{merger} values are corrected for the incompleteness and contamination in the major merger identification and the chance projection effect. The errors are based on Poisson statistics. In addition to the Poisson error, the values in parenthesis include the uncertainties related to F_{comp} , F_{cont} , and N_{proj} .

Hubble follow-up observations. Jiang et al. (2013) have carried out morphological analyses for $z \sim 6$ galaxies with $-22 \lesssim M_{UV} \lesssim -19.5$ based on the visual inspection, reporting that 10 out of 18 bright sources with $M_{UV} \leq -21$ are mergers. Willott et al. (2013) have checked six bright galaxies at $z \sim 6$ detected in the COSMOS *Hubble*/ACS data. Half of the six bright galaxies have multiple components which are likely to be galaxy mergers. Bowler et al. (2017) have visually examined the morphology of 22 $z \sim 7$ bright galaxies with $-23.2 \lesssim M_{UV} \lesssim -21.2$, nine of which are irregular and/or multiple-component systems. We plot the three previous *Hubble* studies on Figure 4. Here, the galaxies of Jiang et al. (2013) and Willott et al. (2013) are assumed to typically have $M_{UV} \sim -21.8$. We divide the galaxies of Bowler et al. (2017) into the $M_{UV} < -22.41$ bright and $M_{UV} = -22 \pm 0.4$ faint samples to match the M_{UV} ranges. As shown in Figure 4, our f_{merger} estimates at $z \sim 6-7$ are consistent with those of these previous *Hubble* studies within the uncertainties, ensuring that our super-resolution technique works well in identifying galaxy mergers at high redshifts.

4.2 Redshift Evolution of Major Merger Fraction

We investigate the redshift evolution of the major merger fractions. To reduce the effect that f_{merger} depends on M_{UV} , we re-estimate f_{merger} in a relatively narrow M_{UV} range of $-23.4 < M_{UV} < -22.8$. Figure 5 and Table 3 present f_{merger} as a function of redshift. Albeit with huge error bars at $z \gtrsim 5$, the major merger fractions tend to increase with increasing redshift, from $f_{\text{merger}} \sim 20\%$ at $z \sim 4$ to $\sim 50\%$ at $z \sim 5$, $\sim 60\%$ at $z \sim 6$ and $\sim 80\%$ at $z \sim 7$.

We compare the redshift evolution of f_{merger} estimated in this work and previous studies. Although methods to identify major mergers are inhomogeneous between this work and previous studies, the comparison enables to grasp the rough evolutionary trend. According to the relation between M_{UV} and stellar mass M_* (e.g., Shibuya et al. 2015; Harikane et al. 2016; Song et al. 2016; Stefanon et al. 2021), our bright dropout galaxies at $z \sim 4-7$ would typically have $\log(M_*/M_\odot) \sim 10-11$. Though galaxy mergers have been actively studied for $z \sim 0-3$ and $\log(M_*/M_\odot) < 10$ galaxies (e.g., Tasca et al. 2014; Mundy et al. 2017; Ferreira et al. 2020), we here compare our f_{merger} estimates with a $z \sim 0-6$ result of Duncan et al. (2019) who have investigated comparably massive galaxies with $\log(M_*/M_\odot) > 10.3$. As in Duncan et al. (2019), our major merger fractions similarly increase with increasing redshift. However, our f_{merger} values appear to be systematically higher than those of Duncan et al. (2019). This

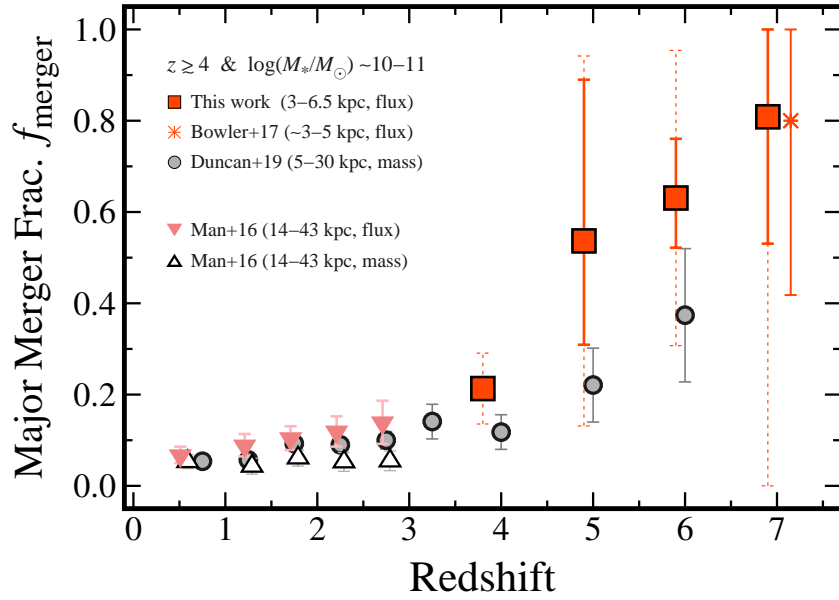


Fig. 5. Redshift evolution of the major merger fraction for massive galaxies. The red squares indicate the bright dropout galaxies with $-23.4 < M_{UV} < -22.8$ in this study. The thick solid error bars are calculated based on Poisson statistics from the galaxy number counts. In addition to the Poisson error, the thin dashed error bars include the uncertainties related to the incompleteness and contamination rate in the galaxy merger identification and the galaxy chance projection effect. The red asterisk represents bright dropout galaxies with $M_{UV} < -22.41$ in Bowler et al. (2017). According to the $M_{UV} - M_*$ relation, the stellar mass of these bright dropout galaxies would be typically $\log(M_*/M_\odot) \sim 10 - 11$. The gray filled circles denote galaxies with $\log(M_*/M_\odot) > 10.3$ in Duncan et al. (2019). The magenta filled inverse triangles and open triangles present f_{merger} for $\log(M_*/M_\odot) > 10.8$ galaxies in Man et al. (2016) based on flux and M_* ratio selections, respectively. Other selection criteria (i.e., the source separation and “flux” or “mass” ratios) are shown in the legends. See Section 4.2 for more details. The data points are slightly offset along the x axis for clarity.

systematic offset might be originated from the difference of major merger selection methods. Man et al. (2016) have estimated f_{merger} based on the flux and M_* ratios for $\log(M_*/M_\odot) > 10.8$ massive galaxies at $z \sim 0 - 3$. While the M_* -ratio based f_{merger} is almost constant at $f_{\text{merger}} \sim 10\%$ in the redshift range of $z \sim 0 - 3$, the flux-ratio based f_{merger} is systematically higher than the M_* -ratio based values by a factor of $\sim 1.5 - 2.5$, and steadily increases with increasing redshift. The difference between the flux- and M_* -ratio based f_{merger} could be linked to, e.g., mass-to-light ratio and gas fractions of faint galaxy components (e.g., Bundy et al. 2009; Hopkins et al. 2010; Lotz et al. 2011; Mantha et al. 2018). If the difference of the selection similarly affects f_{merger} at $z \gtrsim 4$, our flux-ratio based major merger fractions might be comparable to the M_* -ratio based f_{merger} values of Duncan et al. (2019). These results for massive and bright galaxies indicate that the evolutionary trend of f_{merger} at $z \sim 0 - 6$ continues up to a very high redshift of $z \sim 7$, providing insights into physical properties of high- z galaxies, e.g., the high gas fraction and active star-formation at high redshifts (e.g., Tacconi et al. 2018; Liu et al. 2019; Dessauges-Zavadsky et al. 2020).

Some of recent observational and theoretical studies have reported that f_{merger} increases from $z \sim 0$ up to $z \sim 2 - 3$, and subsequently decreases toward high z

(e.g., Ventou et al. 2017; Ventou et al. 2019; Qu et al. 2017; Endsley et al. 2020; O’Leary et al. 2021), possibly due to, e.g., the evolving merger time scale T_{merger} (e.g., Snyder et al. 2017). If f_{merger} intrinsically evolves similar to the decreasing evolutionary trend at $z \gtrsim 3$, f_{merger} of our bright dropout galaxies could be lower than the current f_{merger} estimates. Such low f_{merger} values at $z \sim 4 - 7$ would more strongly support the main conclusion of this study, i.e., the galaxy major merger is not a dominant source for the bright-end DPL shape of galaxy UV LFs (see Section 5).

5 Discussion

We discuss the implications for the shape of galaxy UV LFs with f_{merger} estimated in Section 4.1. In the following subsections, we check whether the number density excess of galaxy UV LFs can be explained by major mergers in two ways: 1) starting from the DPL function (Section 5.1), and 2) starting from the Schechter function (Section 5.2). For the former and the latter, we consider the source blending effect and the number density enhancement resulting from major mergers, respectively. In this study, we make use of $z \sim 4 - 7$ galaxy UV LFs whose AGN contribution has been subtracted (Ono et al. 2018) for the comparison. In

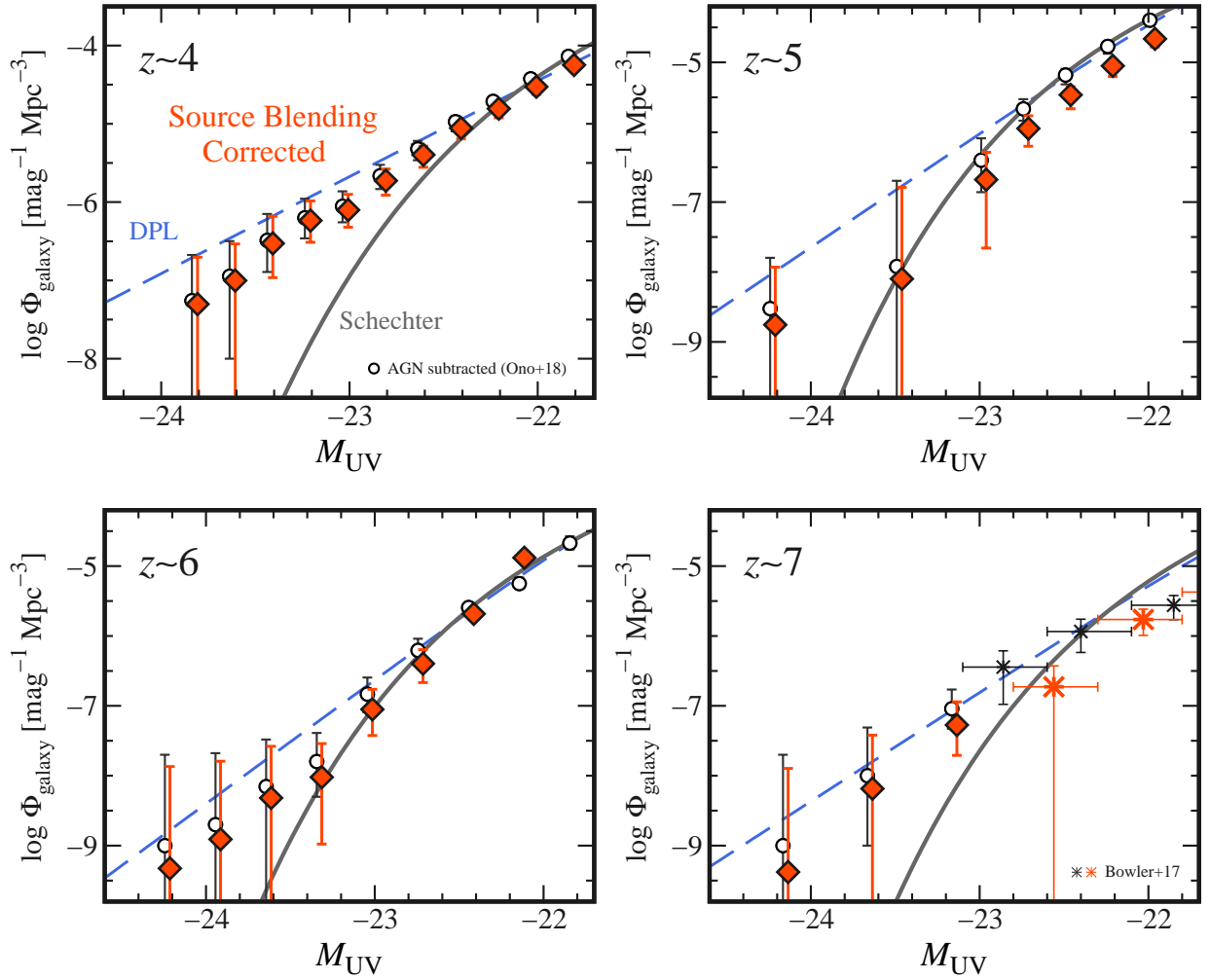


Fig. 6. Galaxy UV LFs at $z \sim 4$ (top left), $z \sim 5$ (top right), $z \sim 6$ (bottom left), and $z \sim 7$ (bottom right). The open circles with error bars indicate galaxy UV LFs whose AGN contribution is subtracted (Ono et al. 2018). The gray solid and blue dashed curves correspond to the best-fit Schechter and DPL functions, respectively (Ono et al. 2018). The red filled diamonds are galaxy UV LFs that are corrected for the source blending effect. For clarity, the red filled diamonds are slightly offset along the x axis. The error bars of the two brightest data points in all the panels reach the Schechter functions because these lower limits are $\Phi_{\text{galaxy}} = 0 \text{ mag}^{-1} \text{ Mpc}^{-3}$. The red large (black small) asterisks at $z \sim 7$ represent the galaxy UV LF in Bowler et al. (2017) that are corrected (not corrected) for the source blending effect.

the redshift range of $z \sim 4-7$, we mainly discuss the galaxy UV LFs at $z \sim 4$ and $z \sim 7$ that have shown the significant number density excess.

5.1 From DPL Function

First, we consider the source blending effect to check whether the number density excess of galaxy UV LFs can be explained by major mergers, starting from the DPL function. Before the discussion, we obtain functional forms of f_{merger} by fitting a linear function of $f_{\text{merger}}(M_{\text{UV}}) = aM_{\text{UV}} + b$ to the f_{merger} values at $z \sim 4$. Here, f_{merger} in Column (2) of Table 2 is used because it is unnecessary to correct for N_{proj} to take into account the source blending effect. The best-fit linear function at $z \sim 4$ is

$f_{\text{merger}}(M_{\text{UV}}) = (0.11 \pm 0.04)M_{\text{UV}} + (2.71 \pm 0.93)$. For the higher redshifts of $z \gtrsim 5$, we fit or scale $f_{\text{merger}}(M_{\text{UV}}) = 0.11M_{\text{UV}} + b$ to the f_{merger} estimates by fixing the parameter of slope $a = 0.11$, because there are few data points at $z \sim 5-7$. The intercepts b at $z \sim (5, 6, 7)$ are $b = (3.07, 3.18, 3.23)$ whose 1σ errors are fixed to that of $z \sim 4$.

Using $f_{\text{merger}}(M_{\text{UV}})$, we correct the observed number density for the source blending effect. In a super-resolution image, a major merger with L_{UV} is separated into a brighter galaxy component with RL_{UV} and a fainter one with $(1-R)L_{\text{UV}}$. Here, R is the luminosity ratio of the brighter galaxy component to the blended single source. According to our super-resolution analysis, we find that the average luminosity ratio is $R = 0.7$ which does not sig-

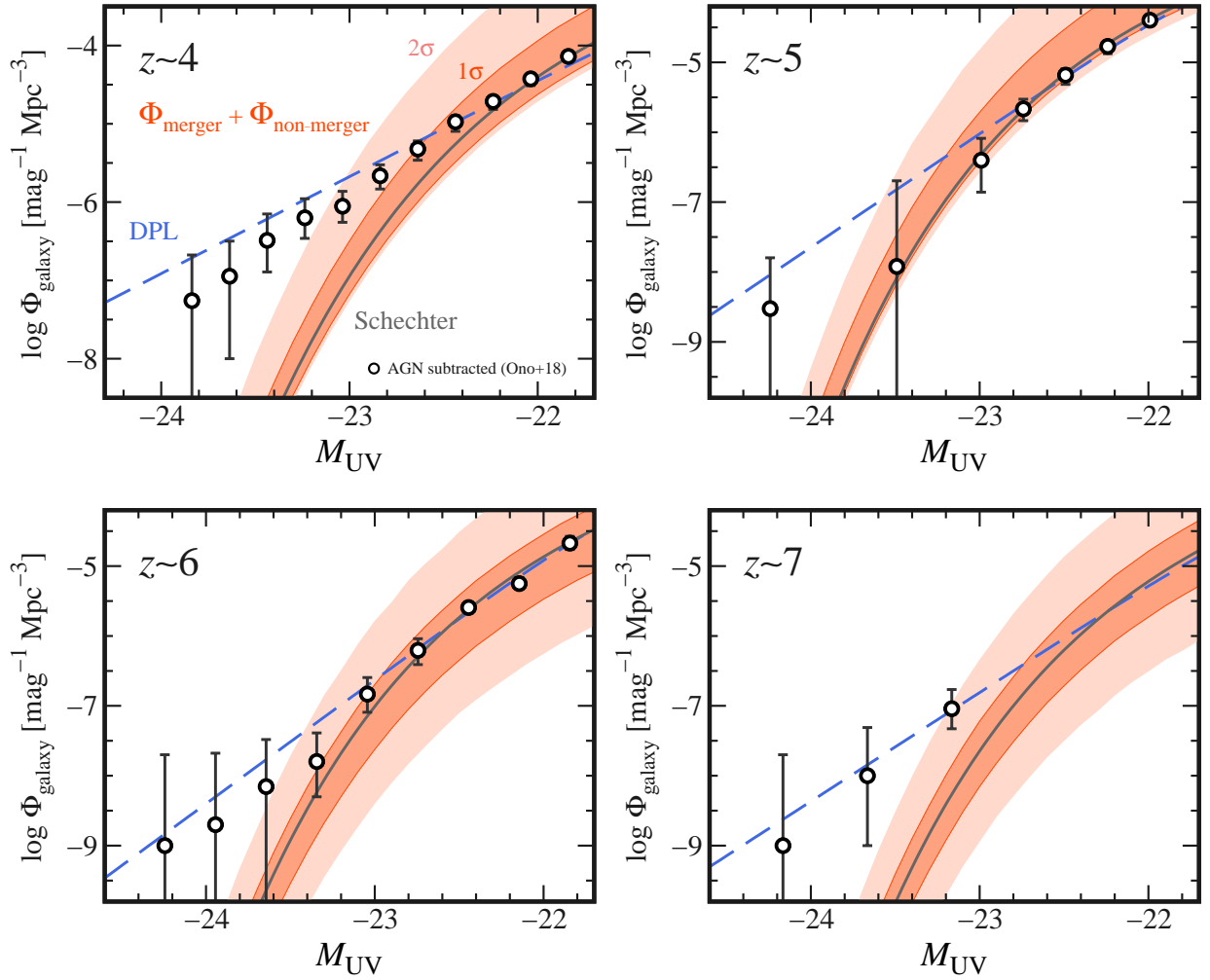


Fig. 7. Same as Figure 6, but for galaxy UV LFs with the number density error regions allowed by the f_{merger} estimates. The dark-red and light-red areas represent the 1σ and 2σ error regions, respectively, of total UV LFs Φ_{tot} that combine two UV LFs of major mergers Φ_m and non-mergers Φ_{nm} (see Section 5.2 for details).

nificantly depend on magnitude and redshift in the entire M_{UV} and z ranges of $-24 \lesssim M_{\text{UV}} \lesssim -22$ and $z \sim 4 - 7$. By combining $f_{\text{merger}}(M_{\text{UV}})$ and R , we count individual de-blended sources, and reconstruct galaxy UV LFs. To scale the original number density and its errors, we use the number of dropout galaxies in the HSC-SSP Wide field (Ono et al. 2018). Here, we simply scale the error bars of the galaxy number density based on the change in galaxy number counts before/after the correction for the source blending effect.

Figure 6 presents the galaxy UV LFs that are corrected for the source blending effect. The number density correction ranges from $\lesssim 0.1$ dex at $z \sim 4$ to ~ 0.5 dex at $z \sim 7$, which is roughly consistent with a *Hubble* study at $z \sim 7$ (Bowler et al. 2017). At $z \sim 4$, the correction slightly reduces the number density of the galaxy UV LF. However, the error bars of number density do not touch the

Schechter function at $-23.4 \lesssim M_{\text{UV}} \lesssim -22.6$. We find that the correction factor tends to be larger at higher z . This trend is originated from high f_{merger} values at high z . In a higher f_{merger} , a larger fraction of galaxies are de-blended into faint components, which decreases the number density more largely compared to lower redshifts. Even at the highest redshift of $z \sim 7$, these correction factors are too small to reach the Schechter functions. In addition, we find some data points of number density “increase” from the original values after the correction at a faint magnitude (e.g., at $M_{\text{UV}} \sim -22$ at $z \sim 6$). A similar trend is found in Bowler et al. (2017). This would be because f_{merger} increases for faint galaxies (see the f_{merger} dependence on magnitude in Figure 4), and many faint de-blended components in a bright M_{UV} bin move into a faint M_{UV} bin. Thus, we conclude that the source blending effect cannot consistently explain the shape of galaxy UV LFs in a wide

magnitude range of $-24 \lesssim M_{UV} \lesssim -22$.

5.2 From Schechter Function

Next, we consider the number density enhancement caused by major mergers to check whether the number density excess of galaxy UV LFs can be explained by major mergers, starting from the Schechter function. As in Section 5.1, we obtain $f_{\text{merger}}(M_{UV}) = aM_{UV} + b$. In contrast to Section 5.1, f_{merger} in Column (3) of Table 2 is used to estimate the intrinsic number density of major mergers. The best-fit linear function at $z \sim 4$ is $f_{\text{merger}}(M_{UV}) = (0.09 \pm 0.04)M_{UV} + (2.31 \pm 0.97)$. The intercepts b at $z \sim (5, 6, 7)$ are $b = (2.66, 2.75, 2.77)$.

Using $f_{\text{merger}}(M_{UV})$, we construct total UV LFs that combines the contributions from major mergers and non-mergers. We incorporate $f_{\text{merger}}(M_{UV})$ into the Schechter function as a function of M_{UV} ,

$$\Phi_{\text{Sch}}(M_{UV}) = \frac{\ln 10}{2.5} \phi^* 10^{-0.4(M_{UV} - M_{UV}^*)(\alpha+1)} \times \exp\left(-10^{-0.4(M_{UV} - M_{UV}^*)}\right), \quad (12)$$

where ϕ^* is the normalization factor in the number density, M_{UV}^* is the characteristic UV magnitude, and α is the faint-end slope. We apply the best-fit Schechter parameters $(\phi^*, M_{UV}^*, \alpha)$ derived in Ono et al. (2018). From the major merger fraction defined as,

$$f_{\text{merger}} \equiv \frac{\Phi_m}{\Phi_{\text{tot}}} \equiv \frac{\Phi_m}{\Phi_m + \Phi_{\text{nm}}}, \quad (13)$$

the total UV LF Φ_{tot} is derived as,

$$\Phi_{\text{tot}} = \Phi_m + \Phi_{\text{nm}} = \frac{1}{1 - f_{\text{merger}}} \Phi_{\text{nm}}, \quad (14)$$

where Φ_m and Φ_{nm} are the UV LFs of major mergers and non-mergers, respectively. All the variables of Φ_{tot} , Φ_m , Φ_{nm} , and f_{merger} are as a function of M_{UV} , which is omitted to avoid the complication of these equations. Because non-merger UV LFs have not been well constrained at high redshifts in previous studies, Φ_{nm} is assumed to be $\Phi_{\text{nm}} = \{1 - f_{\text{merger}}(M_{UV} = -22)\} \Phi_{\text{Sch}}$ where $f_{\text{merger}}(M_{UV} = -22)$ is the major merger fractions estimated for the faint galaxy sample at $M_{UV} = -22$. By varying Φ_{tot} within the $f_{\text{merger}}(M_{UV})$ constraints, we investigate whether the observed number density of galaxy UV LFs can be reproduced with Φ_{tot} .

Figure 7 shows the total UV LFs Φ_{tot} . The 1σ and 2σ error regions of Φ_{tot} are depicted based on Monte-Carlo simulations in which Φ_{tot} is varied within the uncertainty of $f_{\text{merger}}(M_{UV})$. We find that Φ_{tot} is consistent with the observed number density in the galaxy UV LFs within the 2σ uncertainty at a faint UV magnitude of $M_{UV} \gtrsim -23.2$

($L_{UV} \lesssim 8L_{UV}^*$) at $z \sim 4$ and $M_{UV} \gtrsim -23.6$ ($L_{UV} \lesssim 10L_{UV}^*$) at $z \sim 7$, indicating that the DPL shape is partly explained by major mergers. However, an offset in the number density from the total UV LFs still remains at the very bright end of $M_{UV} \lesssim -23.6$ ($L_{UV} \gtrsim 10L_{UV}^*$) at $\sim 2\sigma$ significance.

The discussion in Sections 5.2 and 5.1 indicates that the two effects of the source blending effect and the number density enhancement resulting from major mergers can partly explain the DPL shape at $L_{UV} \sim 3 - 10L_{UV}^*$. However, the DPL shape cannot be explained at the very bright end of $L_{UV} \gtrsim 10L_{UV}^*$. These results would suggest that galaxy major mergers are not enough to reproduce the DPL shape of galaxy UV LFs. This implication has already been obtained from the result of the no f_{merger} enhancement at bright M_{UV} (Section 4.1 and Figure 4). The discussion in this section supports more quantitatively the impacts of galaxy major mergers on the bright-end DPL shape. In addition to galaxy major mergers, other physical mechanisms could contribute to the number density excess of galaxy UV LFs. Possible candidates for these physical mechanisms include 1) insignificant mass quenching and inefficient star-formation/AGN feedback effects in the early Universe (e.g., Binney 1977; Croton et al. 2006; Peng et al. 2010; Ren et al. 2019), 2) low dust obscuration at high- z and the bright end (Bowler et al. 2015; Bowler et al. 2020), 3) gravitational lensing magnification (e.g., Wyithe et al. 2011; Takahashi et al. 2011; Mason et al. 2015; Barone-Nugent et al. 2015). Galaxy selection and analysis biases might affect the the bright-end shape of galaxy UV LFs (e.g., Adams et al. 2020). To reveal the physical mechanisms, it would be important to investigate, e.g., kinematics of inter-stellar/circum-galactic media and dust abundance for bright and massive galaxies, and to compare the contributions from galaxy major mergers and other physical processes.

For future observational studies on galaxy major mergers at $z \gtrsim 4$, analyses with deep IR imaging and spectroscopic data are essential to more accurately estimate f_{merger} at high redshifts. Our method to identify major mergers is not based on the stellar-mass ratio, but just the flux ratio. Although some of our main discussion need only the flux ratio-based f_{merger} (e.g., the source blending effect on galaxy UV LFs), the stellar mass should be measured with deep IR imaging data of, e.g., the *James Webb Space Telescope* to reveal the intrinsic redshift evolution of major merger fractions. In addition, the spectroscopic identification of galaxy pairs is required for more precise f_{merger} estimates without the contamination of chance projection.

6 Summary and Conclusions

We estimate the major merger fractions, f_{merger} , for the bright dropout galaxies at $z \sim 4 - 7$ using the HSC-SSP data and the super-resolution technique. Our super-resolution technique improves the spatial resolution of the ground-based HSC images, from $\sim 0''.6 - 1''.0$ to $\lesssim 0''.1$, which is comparable to that of the *Hubble Space Telescope* (Figures 1 and 2). The combination of the survey capability of HSC and the resolving power allows us to investigate morphological properties of rare galaxy populations at high redshifts. The comparison between the *Hubble* and super-resolution HSC images suggests that we are able to identify $z \sim 4 - 7$ bright major mergers at a high completeness value of $\gtrsim 90\%$ and a relatively low contamination rate of $\sim 20\%$. We apply the super-resolution technique to 6535 very bright dropout galaxies in a high UV luminosity regime of $L_{\text{UV}} \sim 3 - 15 L_{\text{UV}}^*$ (corresponding to $-24 \lesssim M_{\text{UV}} \lesssim -22$) where the number density of galaxies and low-luminosity AGNs is comparable. Our major findings in this study are as follows.

- After the correction for the analysis biases (e.g., the incompleteness of major merger identification), the major merger fractions for the bright dropout galaxies are estimated to be $f_{\text{merger}} \sim 5 - 20\%$ at $z \sim 4$ and $\sim 50 - 80\%$ at $z \sim 5 - 7$. We find no f_{merger} enhancement at $L_{\text{UV}} \sim 3 - 15 L_{\text{UV}}^*$ compared to those of the control sample of faint dropout galaxies with $L_{\text{UV}} \sim 2.5 L_{\text{UV}}^*$ (Figure 4), implying that the major merger is not a dominant source for the bright-end DPL shape of galaxy UV LFs.
- In a relatively narrow M_{UV} range of $-23.4 < M_{\text{UV}} < -22.8$, the major merger fractions show a gradual f_{merger} increase toward high redshift, from $f_{\text{merger}} \sim 20\%$ at $z \sim 4$ to $\sim 50\%$ at $z \sim 5$, $\sim 60\%$ at $z \sim 6$ and $\sim 80\%$ at $z \sim 7$, which is similar to the redshift evolution in f_{merger} found in previous *Hubble* studies (Figure 5). The slight difference in f_{merger} between ours and the previous studies might be interpreted by the difference of merger identification methods, i.e., based on the flux or stellar-mass ratios of galaxy components in merging systems. This result might indicate that the evolutionary trend of f_{merger} continues up to a very high redshift of $z \sim 7$, providing insights into physical properties of high- z galaxies.
- Based on the f_{merger} estimates, we take into account two effects related to major mergers: 1) the source blending effects (Figure 6), and 2) the number density enhancement resulting from major mergers (Figure 7) to check whether the bright-end DPL shape of galaxy UV LFs can be reproduced. While these two effects partly explain the DPL shape at $L_{\text{UV}} \sim 3 - 10 L_{\text{UV}}^*$, the DPL shape can-

not be explained at the very bright end of $L_{\text{UV}} \gtrsim 10 L_{\text{UV}}^*$, even after the AGN contribution is subtracted. The results support scenarios in which other additional mechanisms such as insignificant mass quenching effects, the low dust obscuration, and the gravitational lensing magnification contribute to the DPL shape of galaxy UV LFs at high redshifts.

Acknowledgments

We thank Akio K. Inoue and Marcin Sawicki for useful comments. This work was supported by JSPS KAKENHI Grant Number 20K14508. The Cosmic Dawn Center is funded by the Danish National Research Foundation under grant No. 140. S.F. acknowledges support from the European Research Council (ERC) Consolidator Grant funding scheme (project ConTEst, grant No. 648179). This project has received funding from the European Union's Horizon 2020 research and innovation program under the Marie Skłodowska-Curie grant agreement No. 847523 'INTERACTIONS'.

The HSC collaboration includes the astronomical communities of Japan and Taiwan, and Princeton University. The HSC instrumentation and software were developed by the National Astronomical Observatory of Japan (NAOJ), the Kavli Institute for the Physics and Mathematics of the Universe (Kavli IPMU), the University of Tokyo, the High Energy Accelerator Research Organization (KEK), the Academia Sinica Institute for Astronomy and Astrophysics in Taiwan (ASIAA), and Princeton University. Funding was contributed by the FIRST program from Japanese Cabinet Office, the Ministry of Education, Culture, Sports, Science and Technology (MEXT), the Japan Society for the Promotion of Science (JSPS), Japan Science and Technology Agency (JST), the Toray Science Foundation, NAOJ, Kavli IPMU, KEK, ASIAA, and Princeton University.

This paper makes use of software developed for the Large Synoptic Survey Telescope. We thank the LSST Project for making their code available as free software at <http://dm.lsst.org>.

This paper is based on data collected at the Subaru Telescope and retrieved from the HSC data archive system, which is operated by Subaru Telescope and Astronomy Data Center (ADC) at NAOJ. Data analysis was in part carried out with the co-operation of Center for Computational Astrophysics (CfCA), (CfCA), NAOJ.

The Pan-STARRS1 Surveys (PS1) have been made possible through contributions of the Institute for Astronomy, the University of Hawaii, the Pan-STARRS Project Office, the Max-Planck Society and its participating institutes, the Max Planck Institute for Astronomy, Heidelberg and the Max Planck Institute for Extraterrestrial Physics, Garching, The Johns Hopkins University, Durham University, the University of Edinburgh, Queen's University Belfast, the Harvard-Smithsonian Center for Astrophysics, the Las Cumbres Observatory Global Telescope Network Incorporated, the National Central University of Taiwan, the Space Telescope Science Institute, the National Aeronautics and Space Administration under Grant No. NNX08AR22G issued through

the Planetary Science Division of the NASA Science Mission Directorate, the National Science Foundation under Grant No. AST-1238877, the University of Maryland, and Eotvos Lorand University (ELTE) and the Los Alamos National Laboratory.

This research is based on data collected at Subaru Telescope, which is operated by the National Astronomical Observatory of Japan. We are honored and grateful for the opportunity of observing the Universe from Maunakea, which has the cultural, historical and natural significance in Hawaii.

References

- Adams, N. J., Bowler, R. A. A., Jarvis, M. J., et al. 2020, *MNRAS*, 494, 1771
- Aihara, H., AlSayyad, Y., Ando, M., et al. 2019, *PASJ*, 71, 114
- Aihara, H., Arimoto, N., Armstrong, R., et al. 2018a, *PASJ*, 70, S4
- Aihara, H., Armstrong, R., Bickerton, S., et al. 2018b, *PASJ*, 70, S8
- Akiyama, M., He, W., Ikeda, H., et al. 2018, *PASJ*, 70, S34
- Axelrod, T., Kantor, J., Lupton, R. H., & Pierfederici, F. 2010, in *Society of Photo-Optical Instrumentation Engineers (SPIE) Conference Series*, Vol. 7740, *Software and Cyberinfrastructure for Astronomy*, ed. N. M. Radziwill & A. Bridger, 774015
- Barone-Nugent, R. L., Wyithe, J. S. B., Trenti, M., et al. 2015, *MNRAS*, 450, 1224
- Behroozi, P. S., Zhu, G., Ferguson, H. C., et al. 2015, *MNRAS*, 450, 1546
- Bertin, E. & Arnouts, S. 1996, *A&AS*, 117, 393
- Binney, J. 1977, *ApJ*, 215, 483
- Bluck, A. F. L., Conselice, C. J., Bouwens, R. J., et al. 2009, *MNRAS*, 394, L51
- Bluck, A. F. L., Conselice, C. J., Buitrago, F., et al. 2012, *ApJ*, 747, 34
- Bosch, J., Armstrong, R., Bickerton, S., et al. 2018, *PASJ*, 70, S5
- Bouwens, R. J., Oesch, P. A., Stefanon, M., et al. 2021, *arXiv e-prints*, arXiv:2102.07775
- Bowler, R. A. A., Adams, N. J., Jarvis, M. J., & Häußler, B. 2021, *MNRAS*, 502, 662
- Bowler, R. A. A., Dunlop, J. S., McLure, R. J., et al. 2012, *MNRAS*, 426, 2772
- Bowler, R. A. A., Dunlop, J. S., McLure, R. J., et al. 2015, *MNRAS*, 452, 1817
- Bowler, R. A. A., Dunlop, J. S., McLure, R. J., & McLeod, D. J. 2017, *MNRAS*, 466, 3612
- Bowler, R. A. A., Dunlop, J. S., McLure, R. J., et al. 2014, *MNRAS*, 440, 2810
- Bowler, R. A. A., Jarvis, M. J., Dunlop, J. S., et al. 2020, *MNRAS*, 493, 2059
- Boyd, S., Parikh, N., Chu, E., Peleato, B., & Eckstein, J. 2011, *Foundations and Trends® in Machine Learning*, 3, 1
- Bradley, L. D., Trenti, M., Oesch, P. A., et al. 2012, *ApJ*, 760, 108
- Bundy, K., Fukugita, M., Ellis, R. S., et al. 2009, *ApJ*, 697, 1369
- Calvi, V., Trenti, M., Stiavelli, M., et al. 2016, *ApJ*, 817, 120
- Cibinel, A., Daddi, E., Sargent, M. T., et al. 2019, *MNRAS*, 485, 5631
- Conselice, C. J. & Arnold, J. 2009, *MNRAS*, 397, 208
- Cotini, S., Ripamonti, E., Caccianiga, A., et al. 2013, *MNRAS*, 431, 2661
- Croton, D. J., Springel, V., White, S. D. M., et al. 2006, *MNRAS*, 365, 11
- Curtis-Lake, E., McLure, R. J., Dunlop, J. S., et al. 2016, *MNRAS*, 457, 440
- Dessauges-Zavadsky, M., Ginolfi, M., Pozzi, F., et al. 2020, *A&A*, 643, A5
- Duncan, K., Conselice, C. J., Mundy, C., et al. 2019, *ApJ*, 876, 110
- Ellison, S. L., Mendel, J. T., Patton, D. R., & Scudder, J. M. 2013, *MNRAS*, 435, 3627
- Ellison, S. L., Patton, D. R., Simard, L., & McConnachie, A. W. 2008, *AJ*, 135, 1877
- Endsley, R., Behroozi, P., Stark, D. P., et al. 2020, *MNRAS*, 493, 1178
- Ferreira, L., Conselice, C. J., Duncan, K., et al. 2020, *ApJ*, 895, 115
- Figueiredo, M. A. T. & Bioucas-Dias, J. M. 2010, *IEEE Transactions on Image Processing*, 19, 3133
- Finkelstein, S. L., Ryan, Russell E., J., Papovich, C., et al. 2015, *ApJ*, 810, 71
- Furusawa, H., Koike, M., Takata, T., et al. 2018, *PASJ*, 70, S3
- Grogin, N. A., Kocevski, D. D., Faber, S. M., et al. 2011, *ApJS*, 197, 35
- Guo, Y., Ferguson, H. C., Giavalisco, M., et al. 2013, *ApJS*, 207, 24
- Harikane, Y., Ouchi, M., Ono, Y., et al. 2016, *ApJ*, 821, 123
- Harikane, Y., Ouchi, M., Ono, Y., et al. 2018, *PASJ*, 70, S11
- Hopkins, P. F., Younger, J. D., Hayward, C. C., Narayanan, D., & Hernquist, L. 2010, *MNRAS*, 402, 1693
- Ivezić, Ž., Kahn, S. M., Tyson, J. A., et al. 2019, *ApJ*, 873, 111
- Jiang, L., Egami, E., Fan, X., et al. 2013, *ApJ*, 773, 153
- Jurić, M., Kantor, J., Lim, K. T., et al. 2017, in *Astronomical Society of the Pacific Conference Series*, Vol. 512, *Astronomical Data Analysis Software and Systems XXV*, ed. N. P. F. Lorente, K. Shortridge, & R. Wayth, 279
- Kawamata, R., Ishigaki, M., Shimasaku, K., Oguri, M., & Ouchi, M. 2015, *ApJ*, 804, 103
- Kawanomoto, S., Uruguchi, F., Komiyama, Y., et al. 2018, *PASJ*, 70, 66
- Koekemoer, A. M., Faber, S. M., Ferguson, H. C., et al. 2011, *ApJS*, 197, 36
- Komiyama, Y., Obuchi, Y., Nakaya, H., et al. 2018, *PASJ*, 70, S2
- Lackner, C. N., Silverman, J. D., Salvato, M., et al. 2014, *AJ*, 148, 137
- Le Fèvre, O., Abraham, R., Lilly, S. J., et al. 2000, *MNRAS*, 311, 565
- Le Fèvre, O., Béthermin, M., Faisst, A., et al. 2020, *A&A*, 643, A1
- Leauthaud, A., Massey, R., Kneib, J.-P., et al. 2007, *ApJS*, 172,

- 219
- Liu, D., Schinnerer, E., Groves, B., et al. 2019, *ApJ*, 887, 235
- Lotz, J. M., Jonsson, P., Cox, T. J., et al. 2011, *ApJ*, 742, 103
- Lotz, J. M., Madau, P., Giavalisco, M., Primack, J., & Ferguson, H. C. 2006, *ApJ*, 636, 592
- Lucy, L. B. 1974, *AJ*, 79, 745
- Man, A. W. S., Zirm, A. W., & Toft, S. 2016, *ApJ*, 830, 89
- Mantha, K. B., McIntosh, D. H., Brennan, R., et al. 2018, *MNRAS*, 475, 1549
- Mason, C. A., Treu, T., Schmidt, K. B., et al. 2015, *ApJ*, 805, 79
- Matsuoka, Y., Iwasawa, K., Onoue, M., et al. 2019, *ApJ*, 883, 183
- McLeod, D. J., McLure, R. J., & Dunlop, J. S. 2016, *MNRAS*, 459, 3812
- McLure, R. J., Dunlop, J. S., Bowler, R. A. A., et al. 2013, *MNRAS*, 432, 2696
- Miyazaki, S., Komiyama, Y., Kawanomoto, S., et al. 2018, *PASJ*, 70, S1
- Miyazaki, S., Komiyama, Y., Nakaya, H., et al. 2012, in *Society of Photo-Optical Instrumentation Engineers (SPIE) Conference Series*, Vol. 8446, Ground-based and Airborne Instrumentation for Astronomy IV, ed. I. S. McLean, S. K. Ramsay, & H. Takami, 84460Z
- Mundy, C. J., Conselice, C. J., Duncan, K. J., et al. 2017, *MNRAS*, 470, 3507
- Oesch, P. A., Bouwens, R. J., Carollo, C. M., et al. 2010a, *ApJL*, 725, L150
- Oesch, P. A., Bouwens, R. J., Carollo, C. M., et al. 2010b, *ApJL*, 709, L21
- Oesch, P. A., Bouwens, R. J., Illingworth, G. D., et al. 2013, *ApJ*, 773, 75
- Oke, J. B. 1974, *ApJS*, 27, 21
- Oke, J. B. & Gunn, J. E. 1983, *ApJ*, 266, 713
- O’Leary, J. A., Moster, B. P., Naab, T., & Somerville, R. S. 2021, *MNRAS*, 501, 3215
- Ono, Y., Ouchi, M., Harikane, Y., et al. 2018, *PASJ*, 70, S10
- Ostriker, J. P. & Tremaine, S. D. 1975, *ApJL*, 202, L113
- Parsa, S., Dunlop, J. S., McLure, R. J., & Mortlock, A. 2016, *MNRAS*, 456, 3194
- Patton, D. R., Carlberg, R. G., Marzke, R. O., et al. 2000, *ApJ*, 536, 153
- Peng, Y.-j., Lilly, S. J., Kovač, K., et al. 2010, *ApJ*, 721, 193
- Qu, Y., Helly, J. C., Bower, R. G., et al. 2017, *MNRAS*, 464, 1659
- Ravindranath, S., Giavalisco, M., Ferguson, H. C., et al. 2006, *ApJ*, 652, 963
- Ren, K., Trenti, M., & Mason, C. A. 2019, *ApJ*, 878, 114
- Richardson, W. H. 1972, *Journal of the Optical Society of America* (1917-1983), 62, 55
- Rudin, L. I., Osher, S., & Fatemi, E. 1992, *Physica D Nonlinear Phenomena*, 60, 259
- Sawicki, M., Arcila-Osejo, L., Golob, A., et al. 2020, *MNRAS*, 494, 1366
- Schechter, P. 1976, *ApJ*, 203, 297
- Shibuya, T., Ouchi, M., & Harikane, Y. 2015, *ApJS*, 219, 15
- Shibuya, T., Ouchi, M., Kubo, M., & Harikane, Y. 2016, *ApJ*, 821, 72
- Snyder, G. F., Lotz, J. M., Rodriguez-Gomez, V., et al. 2017, *MNRAS*, 468, 207
- Song, M., Finkelstein, S. L., Ashby, M. L. N., et al. 2016, *ApJ*, 825, 5
- Stefanon, M., Bouwens, R. J., Labbé, I., et al. 2021, arXiv e-prints, arXiv:2103.16571
- Stefanon, M., Labbé, I., Bouwens, R. J., et al. 2017, *ApJ*, 851, 43
- Stefanon, M., Labbé, I., Bouwens, R. J., et al. 2019, *ApJ*, 883, 99
- Steidel, C. C., Adelberger, K. L., Giavalisco, M., Dickinson, M., & Pettini, M. 1999, *ApJ*, 519, 1
- Stevens, M. L., Finkelstein, S. L., Wold, I., et al. 2018, *ApJ*, 863, 63
- Tacconi, L. J., Genzel, R., Saintonge, A., et al. 2018, *ApJ*, 853, 179
- Takahashi, R., Oguri, M., Sato, M., & Hamana, T. 2011, *ApJ*, 742, 15
- Tanaka, M., Coupon, J., Hsieh, B.-C., et al. 2018, *PASJ*, 70, S9
- Tasca, L. A. M., Le Fèvre, O., López-Sanjuan, C., et al. 2014, *A&A*, 565, A10
- Tibshirani, R. 1996, *Journal of the Royal Statistical Society. Series B (Methodological)*, 58, 267
- Toshikawa, J., Uchiyama, H., Kashikawa, N., et al. 2018, *PASJ*, 70, S12
- Ventou, E., Contini, T., Bouché, N., et al. 2017, *A&A*, 608, A9
- Ventou, E., Contini, T., Bouché, N., et al. 2019, *A&A*, 631, A87
- Wen, Y., Chan, R. H., & Zeng, T. 2016, *Science China Mathematics*, 59, 141
- Willott, C. J., McLure, R. J., Hibon, P., et al. 2013, *AJ*, 145, 4
- Wong, K. C., Blanton, M. R., Burles, S. M., et al. 2011, *ApJ*, 728, 119
- Wyithe, J. S. B., Yan, H., Windhorst, R. A., & Mao, S. 2011, *Nature*, 469, 181

7 Appendix

In this appendix, we briefly explain how to solve Equation (3) with the Augmented Lagrangian (Equation 5). Based on the standard ADMM procedure (Boyd et al. 2011), we divide the problem of the RL deconvolution into subproblems for the PSF convolution, the Poisson noise, and the flux non-negativity. Using the proximal operator **prox**, we iteratively update the \mathbf{x} , \mathbf{w}_1 , \mathbf{w}_2 , and \mathbf{h} (i.e., \mathbf{u}) vectors as follows,

$$\begin{aligned}\mathbf{x} &\leftarrow \mathbf{prox}_q(\mathbf{v}) = \arg \min_{\{\mathbf{x}\}} L_\rho(\mathbf{x}, \mathbf{w}, \mathbf{h}) \\ &= \arg \min_{\{\mathbf{x}\}} \frac{1}{2} \|\mathbf{Ax} - \mathbf{w}\|_2^2, \\ \mathbf{v} &= \mathbf{w} - \mathbf{u}\end{aligned}\tag{15}$$

$$\mathbf{w}_1 \leftarrow \mathbf{prox}_{p,\rho}(\mathbf{v}) = \arg \min_{\{\mathbf{w}_1\}} L_\rho(\mathbf{x}, \mathbf{w}, \mathbf{h})$$

$$\begin{aligned}
&= \arg \min_{\{\mathbf{w}_1\}} -\log p(\mathbf{y}|\mathbf{w}_1) + \frac{\rho}{2} \|\mathbf{v} - \mathbf{w}_1\|_2^2, \\
&\mathbf{v} = \mathbf{P}\mathbf{x} + \mathbf{u}_1
\end{aligned} \tag{16}$$

$$\begin{aligned}
\mathbf{w}_2 \leftarrow \text{prox}_{i,\rho}(\mathbf{v}) &= \arg \min_{\{\mathbf{w}_2\}} L_\rho(\mathbf{x}, \mathbf{w}, \mathbf{h}) \\
&= \arg \min_{\{\mathbf{w}_2\}} I_{R_+}(\mathbf{w}_2) + \frac{\rho}{2} \|\mathbf{v} - \mathbf{w}_2\|_2^2, \\
&\mathbf{v} = \mathbf{x} + \mathbf{u}_2
\end{aligned} \tag{17}$$

$$\begin{bmatrix} \mathbf{u}_1 \\ \mathbf{u}_2 \end{bmatrix} \leftarrow \mathbf{u} + \mathbf{A}\mathbf{x} - \mathbf{w} \tag{18}$$

where \mathbf{u} is the scaled Lagrange multiplier $\mathbf{u} = (1/\rho)\mathbf{h}$. In the following paragraphs, we derive the proximal operators for the \mathbf{x} , \mathbf{w}_1 , and \mathbf{w}_2 updates in Equations (15)-(17).

For the \mathbf{x} update: The proximal operator for the \mathbf{x} update is formulated as the solution of the quadratic problem,

$$\begin{aligned}
\text{prox}_q(\mathbf{v}) &= \arg \min_{\{\mathbf{x}\}} \frac{1}{2} \left\| \begin{bmatrix} \mathbf{P} \\ \mathbf{I} \end{bmatrix} \mathbf{x} - \begin{bmatrix} \mathbf{v}_1 \\ \mathbf{v}_2 \end{bmatrix} \right\|_2^2 \\
&= (\mathbf{P}^T \mathbf{P} + \mathbf{I})^{-1} (\mathbf{P}^T \mathbf{v}_1 + \mathbf{v}_2) \\
&= \frac{c * v_1 + v_2}{c * c + 1}
\end{aligned} \tag{19}$$

where c is the PSF convolution kernel.

For the \mathbf{w}_1 update: Next, we derive the proximal operator for the \mathbf{w}_1 update. Using Equation (1), the objective function in Equation (16) is rewritten as

$$J(\mathbf{w}_1) = -\log(\mathbf{w}_1)^T \mathbf{y} + \mathbf{w}_1^T \mathbf{1} + \frac{\rho}{2} (\mathbf{w}_1 - \mathbf{v})^T (\mathbf{w}_1 - \mathbf{v}) \tag{20}$$

We equate the gradient of the objective function $J(\mathbf{w}_1)$ to zero,

$$\begin{aligned}
\frac{\partial J}{\partial \mathbf{w}_1} &= -\frac{\mathbf{y}}{\mathbf{w}_1} + \mathbf{1} + \rho(\mathbf{w}_1 - \mathbf{v}) \\
&= \mathbf{w}_1^2 + \frac{1 - \rho \mathbf{v}}{\rho} \mathbf{w}_1 - \frac{\mathbf{y}}{\rho} = 0.
\end{aligned} \tag{21}$$

By solving this classical root-finding problem of the quadratic equation, we formulate the proximal operator as,

$$\text{prox}_{p,\rho}(\mathbf{v}) = \frac{1 - \rho \mathbf{v}}{2\rho} + \sqrt{\left(\frac{1 - \rho \mathbf{v}}{2\rho}\right)^2 + \frac{\mathbf{y}}{\rho}}. \tag{22}$$

For the \mathbf{w}_2 update: The proximal operator for the \mathbf{w}_2 updates can be formulated as

$$\begin{aligned}
\text{prox}_{i,\rho}(\mathbf{v}) &= \arg \min_{\{\mathbf{w}_2\}} I_{R_+}(\mathbf{w}_2) + \frac{\rho}{2} \|\mathbf{v} - \mathbf{w}_2\|_2^2 \\
&= \arg \min_{\{\mathbf{w}_2\}} \|\mathbf{v} - \mathbf{w}_2\|_2^2 \\
&= \Pi_{R_+}(\mathbf{v})
\end{aligned} \tag{23}$$

where Π_{R_+} is defined as follows,

$$\Pi_{R_+}(\mathbf{v}_j) = \begin{cases} 0 & \mathbf{v}_j < 0 \\ \mathbf{v}_j & \mathbf{v}_j \geq 0 \end{cases} \tag{24}$$

After the convergence of the iteration in Equations (15)-(18), we obtain the restored image \mathbf{x} .